Application of 3D Printing for Smart Objects with Embedded Electronic Sensors and Systems

Hiroki Ota, Sam Emaminejad, Yuji Gao, Allan Zhao, Eric Wu, Samyuktha Challa, Kevin Chen, Hossain M. Fahad, Amit K. Jha, Daisuke Kiriya, Wei Gao, Hiroshi Shiraki, Kazuhito Morioka, Adam R. Ferguson, Kevin E. Healy, Ronald W. Davis, and Ali Javey*

Dr. H. Ota, Dr. S. Emaminejad, Y. Gao, A. Zhao, E. Wu, K. Chen, Dr. H. M. Fahad, Dr. D. Kiriya, Dr. W. Gao, H. Shiraki, Prof. A. Javey: Electrical Engineering and Computer Sciences University of California Berkeley , CA 94720 , USA E-mail: ajavey@eecs.berkeley.edu; Dr. H. Ota, Dr. S. Emaminejad, Y. Gao, K. Chen, Dr. H. M. Fahad, Dr. D. Kiriya, Dr. W. Gao, H. Shiraki, Prof. A. Javey: Berkeley Sensor and Actuator Center University of California Berkeley , CA 94720 , USA; Dr. H. Ota, Dr. S. Emaminejad, Y. Gao, K. Chen, Dr. H. M. Fahad, Dr. D. Kiriya, Dr. W. Gao, H. Shiraki, Prof. A. Javey:: Materials Sciences Division Lawrence Berkeley National Laboratory Berkeley , CA 94720 , USA; Dr. S. Emaminejad, S. Challa, Prof. R. W. Davis: Stanford Genome Technology Center Stanford School of Medicine 3165 Porter Drive , Palo Alto , CA 94304 , USA; Y. Gao: Mechanical Engineering Tianjin University 92 Weijin Road , Nankai, Tianjin 300072 , P.R. China; Dr. A. K. Jha, Prof. K. E. Healy: Bioengineering University of California Berkeley , CA 94720 , USA; Dr. A. K. Jha, Prof. K. E. Healy: Material Science and Engineering University of California Berkeley , CA 94720 , USA; Dr. K. Morioka, Prof. A. R. Ferguson: Neurological Surgery University of California San Francisco , 1001 Potrero Avenue , CA 94110 , USA

Abstract

Applications of a 3D printing process are presented. This process integrates liquid-state printed components and interconnects with IC chips in all three dimensions, various orientations, and multiple printing layers to deliver personalized system-level functionalities. As an example application, a form-fitting glove is demonstrated with embedded programmable heater, temperature sensor, and the associated control electronics for thermotherapeutic treatment.

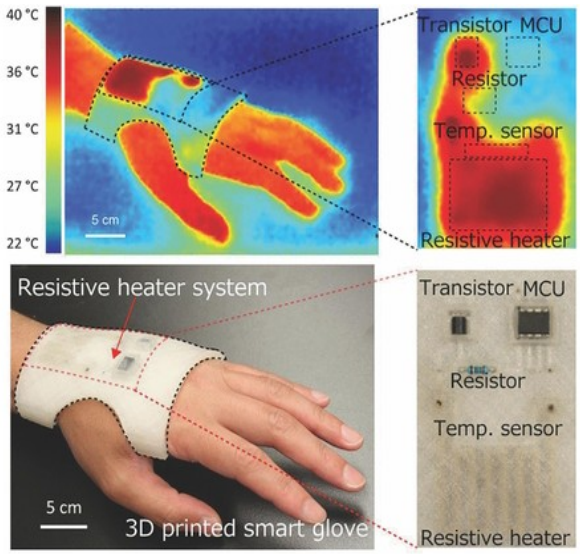

Aligned with the vision of “Internet of Things,” it is expected that the number of interconnected devices, equipped with sensing and actuation functionalities, will grow beyond trillions of units by 2025,[1] representing about 1000 devices per person in the world. The need for personalization that inevitably ensues necessitates devising novel manufacturing processes that seamlessly integrate such functionalities into our surrounding objects. To this end, 3D printing is an excellent process, as it is capable of rapid and on-demand production of mechanically sophisticated and personalized objects with efficient use of materials.[2-8] To enable 3D printing of electronic sensors and systems, conductive materials need to be incorporated in the printing process. Previously, patterning of liquid metals by direct writing[9] and filling predefined microchannels has been demonstrated.[10-12] Furthermore, the use of liquid metal as conductors,[13, 14] capacitors,[15] and antennas[16-24] has been shown. The illustrated circuit and sensor applications include embedded elastomer conductors,[13] hyperelastic pressure sensors,[10] stretchable radiation sensors,[17] passive wireless sensors,[11] deformable and tunable fluidic antennas,[25] and tactile interfaces.[26]

Given these advances, 3D printing can now be exploited to develop 3D electronic systems embedded within printed objects that facilitate personalized sensing and actuation functionalities. To illustrate this capability, we particularly demonstrate 3D printing of two fully integrated objects that deliver various sensing, actuation, and signal processing operations. These objects embed liquid metal-based passive/active components and commercially available silicon integrated circuits (ICs) to achieve the envisioned functionalities. The first object demonstrates the capability of 3D printing approach to embed multilayer electronic circuit boards within 3D structures. The second object demonstrates the application of 3D printing process to deliver wearable platforms that are specifically tailored to an individual's body and needs. Specifically, a form-fitting glove is developed with embedded programmable heater, temperature sensor, and

the associated control electronics for thermotherapeutic treatment. The process enables assembly of electronic components into complex 3D architectures and provides a new platform for creating personalized smart objects.

As exemplified in Figure 1a, conductive channels are printed within an object (e.g., a glove) in various configurations to realize 3D liquid-state sensors, actuators, and circuit components (resistors, capacitors, and antennas). These components can be tunably printed within both stretchable and rigid substrates and can provide standalone functionalities. The channels are also used as interconnects to integrate readily available silicon IC chips and realize fully embedded systems inside the printed object. Integration of silicon IC chips enables advanced circuit functionalities that would not have been achieved otherwise by 3D printed liquid-state components alone. Figure 1b–e illustrates the corresponding fabrication scheme. First, as shown in Figure 1b, a base substrate, containing microchannels and slots for the integrated components, is fabricated by a 3D printer (MakerGear and Leapfrog). Second, the microchannels are injected with liquid metal to form the liquid-based circuit components, devices, and interconnects (Figure 1c). Third, IC chips and other solid state electronic components including discrete resistors and capacitors are embedded within the substrate slots. The terminals of these components are inserted into the microchannels to form electrical connection with the liquid metal interconnects. In order to obtain a flat top layer, poly(dimethylsiloxane) (PDMS) and epoxy resin are poured onto the inserted components (Figure 1d). The 3D fabrication process is then continued (Figure 1e) to print the subsequent layers in the design by repeating the previous steps (Figure 1b).

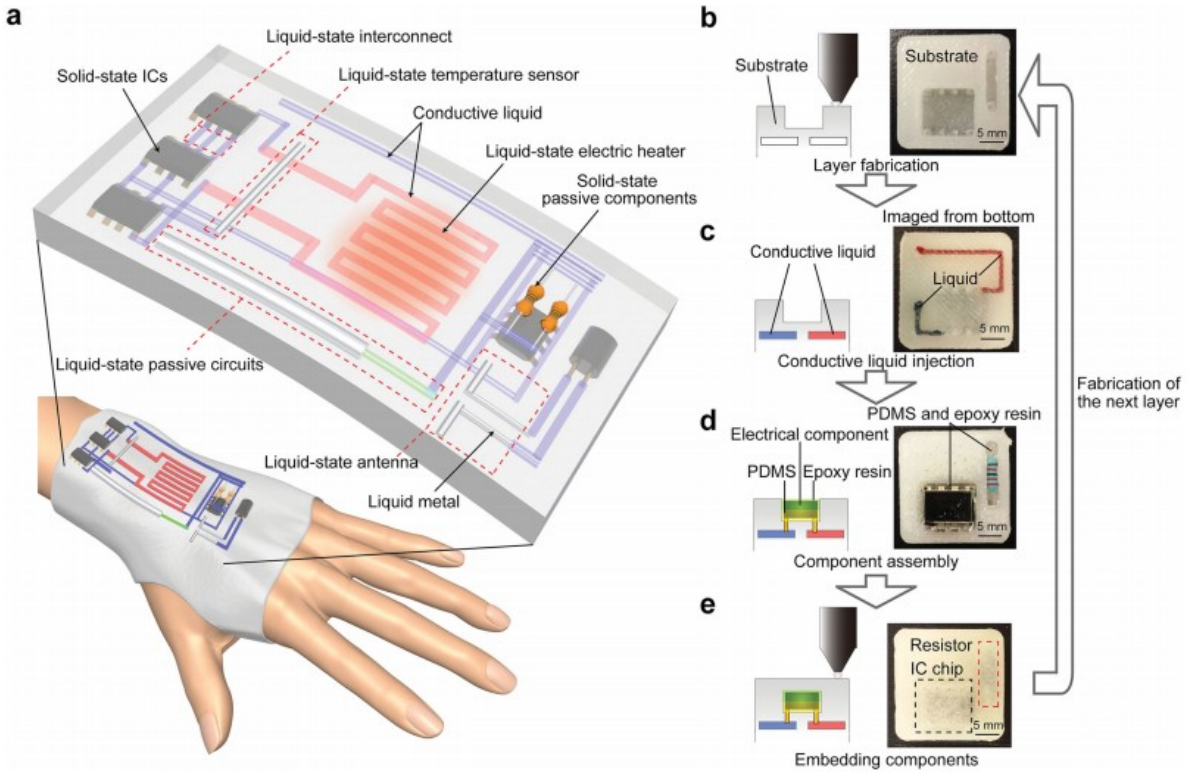

Figure 1. a) The multilayer schematic of a 3D printed smart object which integrates advanced IC chips and other solid state components, as well as liquid-state circuit components and liquid metal interconnects. b–e) The fabrication process flow of a given layer including: b) substrate fabrication, c) conductive liquid injection, d) component assembly, and e) embedding of components.

The presented approach can be geared toward creating both stretchable and rigid objects. The elastic objects can particularly be used in form-fitting applications that need to preserve their functionalities despite experiencing strains due to bending and deformation (Figure S1, Supporting Information). Additionally, our approach allows for tunable creation of circuit components with standalone functionalities. The dimensions and electrical properties of such components can be simply altered through minimal change in the software code or use of a different channel filling material. Accordingly, we have demonstrated our process capabilities in three contexts of constructing twistable wires, antennas, as well as circuit components (resistors and capacitors) that were configured to realize passive filters.

First, to demonstrate the process capability for printing stretchable objects, two highly twistable Galinstan-based channels were printed in the form of a double helix structure, serving as a pair of wires. The wires interfaced a discrete light-emitting diode (LED; Figures S1 and S2, Supporting Information). As shown in Figure 2a,b, the LED is fully operational and emits light with no change in intensity despite the pair of wires being twisted by up to 540°. Second, to demonstrate the tunability of the fabrication process, a set of 3D printed dipole antennas with varying dipole lengths were printed, using Galinstan as the conductive material (Figure 2c,d). The characterization results for the corresponding antennas are presented in

Figure 2d and Figure S3 (Supporting Information), indicating that the antenna resonant frequency and the antenna length have an inverse relationship as expected. These results demonstrate the precise tunability in fabrication of the 3D printed antennas. To illustrate the practical utility, the 24.5 mm antenna was installed in both a video transmitter and a receiver, to wirelessly transmit video content from a camera to a laptop (Figure 2e and Figure S4, Supporting Information). Third, we applied our approach to tunably realize embedded passive circuit elements (e.g., resistors and capacitors). These elements were used to construct a set of 3D printed low- and high-pass filters (LPFs and HPFs) with varying cut-off frequencies. To this end, we created liquid-state resistor and capacitor components. For the resistor material we used silicone oil, containing 20% carbon black. Here, the resistivity of the liquid-state resistor can be modulated from 5×10^{-5} Ωm to 100 Ωm by adopting different materials of varying suspension densities in the channels' liquid composition (Figure S5a–c, Supporting Information). For the interconnects and capacitor's inner/outer plates we used Galinstan as the conductive material. To realize the capacitive element, we used a structure similar to that of a conventional cylindrical capacitor geometry. Shrinking the radial spacing between the inner and outer plates allows achieving capacitance per length of up to 10 pF cm^{-1} (Figure S5d–f, Supporting Information). Through embedding these resistor and capacitor components (Figure S6, Supporting Information) in a series configuration, LPF and HPF were realized (Figure 2f–h). We could modulate the cut-off frequency of the filter by changing the resistor and capacitor values. For example, the capacitance is modulated through the use of cylindrical capacitors of different axial lengths. Depending on the end application requirements, the same fabrication process can be applied to construct similar circuits in 2D (as shown in Figure S7, Supporting Information).

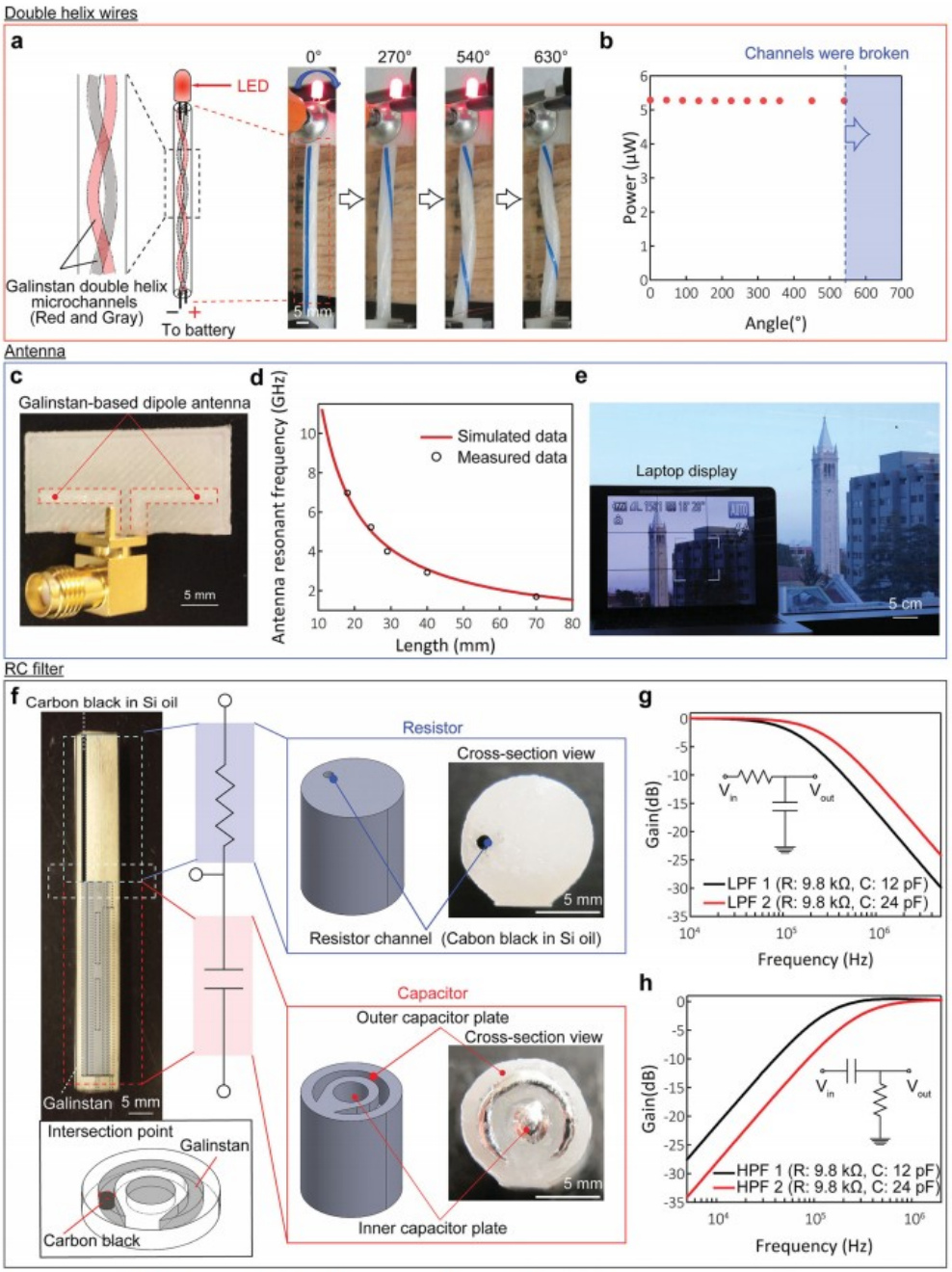

Figure 2. a) Schematic and optical images of a twistable LED connected via a double helix Galinstan microchannel. The device was twisted up to 630°. b) Stability of the emitted light intensity power of the LED undergoing twisting. No change in the LED's light intensity was observed despite being twisted by up to 540° (beyond which the channels physically broke). c) An optical image of a representative 3D printed dipole antenna connected to an SMA connector. d) Resonant frequencies of the 3D printed antennas with respect to the corresponding individual antenna length (measured vs simulated). e) A screenshot of the video content that was transmitted and received in real-time by two 24.5 mm dipole antennas (as captured by a camera and displayed on a laptop). f) Optical and schematic images of the 3D printed cylindrical high- and low-pass filters. The filter is composed of a liquid-state resistor (blue box) and a cylindrical capacitor (red box). Two components are connected inside the structure (gray box) and form a series combination of the resistor and capacitor. g) Frequency response of the low-pass filter for two representative series combination ($R = 9.8$ kΩ, $C = 12$ pF and $R = 9.8$ kΩ, $C = 24$ pF). h) Frequency response of the high-pass filter for two representative series combination ($R = 9.8$ kΩ, $C = 12$ pF and $R = 9.8$ kΩ, $C = 24$ pF).

Furthermore, our approach can be used to print embedded systems within objects through a multilayer process. Here, the embedded system was incorporated in a structure resembling the Sather Tower of University of

California, Berkeley. As a proof-of-concept, we implemented a photodetection platform using fully embedded current sensing circuitry that conditions and processes the current output of an externally connected phototransistor. As shown in Figure 3a,b, to create this platform, three interconnected circuits were implemented in three different layers. The discrete ICs and peripheral passive components were connected by the 3D printed in-plane and vertical liquid metal interconnects. These circuits implement: (1) a transimpedance amplifier (TIA) that converts the phototransistor's output current signal to voltage, (2) an LPF that minimizes the high frequency noise and interference, and (3) a microcontroller unit (MCU) as a digital readout. The corresponding schematic views are included in Figure 3b and Figure S8 (Supporting Information). The MCU, LPF, and TIA circuits were embedded as part of the first, second, and third layers of the fabrication procedure, respectively. The 3D embedding capability of the process also enables insertion of components in various spatial orientations, thus creating new degrees of freedom in design of embedded systems. For example, in this implementation, the TIA chip is placed at a 90° angle relative to the fabrication plane. Figure 3c,d, respectively, illustrates the drawing of the originally envisioned 3D system and the final 3D printed design with embedded electronics inside. The X-ray imaging (Figure 3e) shows the proper 3D placement and connection of circuit elements within the printed tower. We verified the implemented photodetection functionality by shining an LED light source on the phototransistor, and varying the light intensity. As shown in Figure 3f, the output voltage of the system is linearly proportional to the input light intensity. The system's photodetection functionality was further validated by periodically turning the light source on and off and correspondingly reading low and high MCU output values (Figure 3g). Depending on the end application requirements, this fabrication process can be equivalently applied to implement 2D embedded systems (Figure S9, Supporting Information).

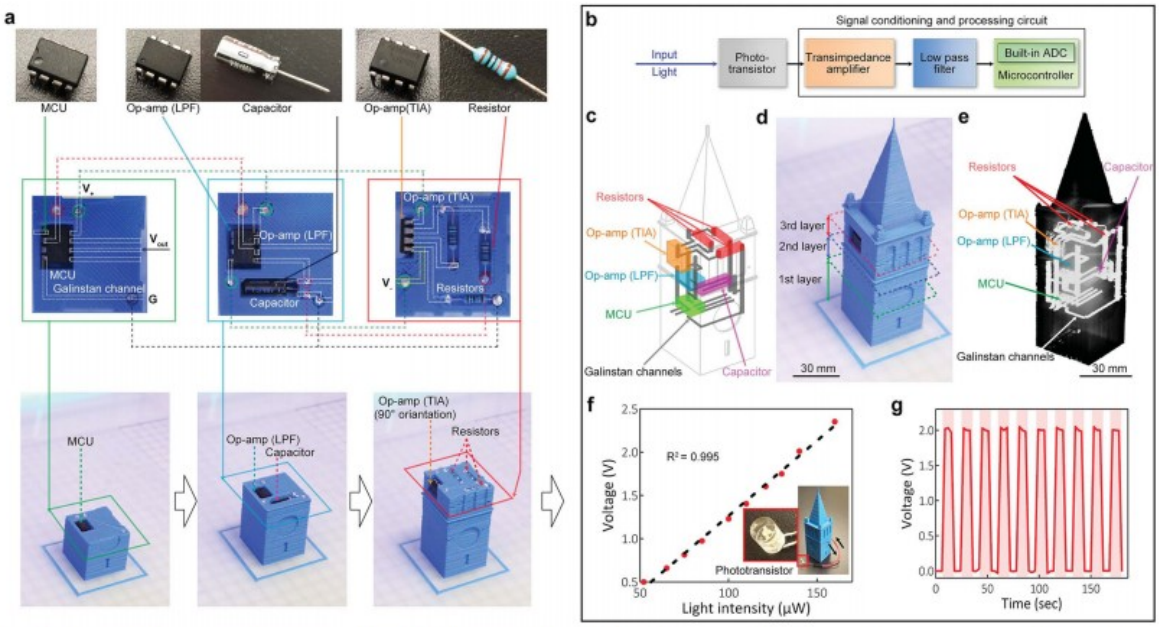

Figure 3. a) Layer-by-layer fabrication process to embed microcontroller unit (MCU), low-pass filter (LPF), and transimpedance amplifier (TIA) circuit configurations inside the tower structure. The electrical connections between the components are achieved via conductive Galinstan microchannels. b) System-level block diagram of the photodetection system showing the signal transduction (externally connected phototransistor), conditioning (TIA and LPF), and processing (MCU) path. c) 3D drawing of the miniature Sather Tower illustrating the spatial placement of the circuit components as well as the in-plane and vertical Galinstan interconnects. d) Optical image of the 3D printed photodetection system embedded inside the tower. e) Corresponding X-ray image of the tower. White segments are discrete ICs and passive circuit components as well as Galinstan interconnects. f) Linear output response with respect to the input light intensity. g) Temporal output response as the input light source is being periodically switched on and off (the on-states of the light source are depicted by semi-transparent red boxes).

The unique capabilities demonstrated by the presented process, in terms of rapid 3D printing of embedded sensors, actuators, and systems, are well aligned with applications where on-demand creation of customized objects is required. Furthermore, by using stretchable materials in the 3D printing process of the structure, we can create form-fitting objects that are amenable for wearable applications. The presented fabrication scheme can specifically be applied in point-of-care settings to create smart physical assisting and therapeutic wearable devices that are personalized and tailored to the patient's condition and body. To this end, we developed a customized hand glove with an integrated programmable heater and a temperature sensor (Figure 4a,b). This glove can be worn by patients in need of thermotherapy, where application of heat at the point of injury is required to enhance blood flow and reduce pain.[27] This wearable system should be specifically tailored to the patient's hand to ensure that it can be comfortably worn for a prolonged period of time in order to achieve effective results.

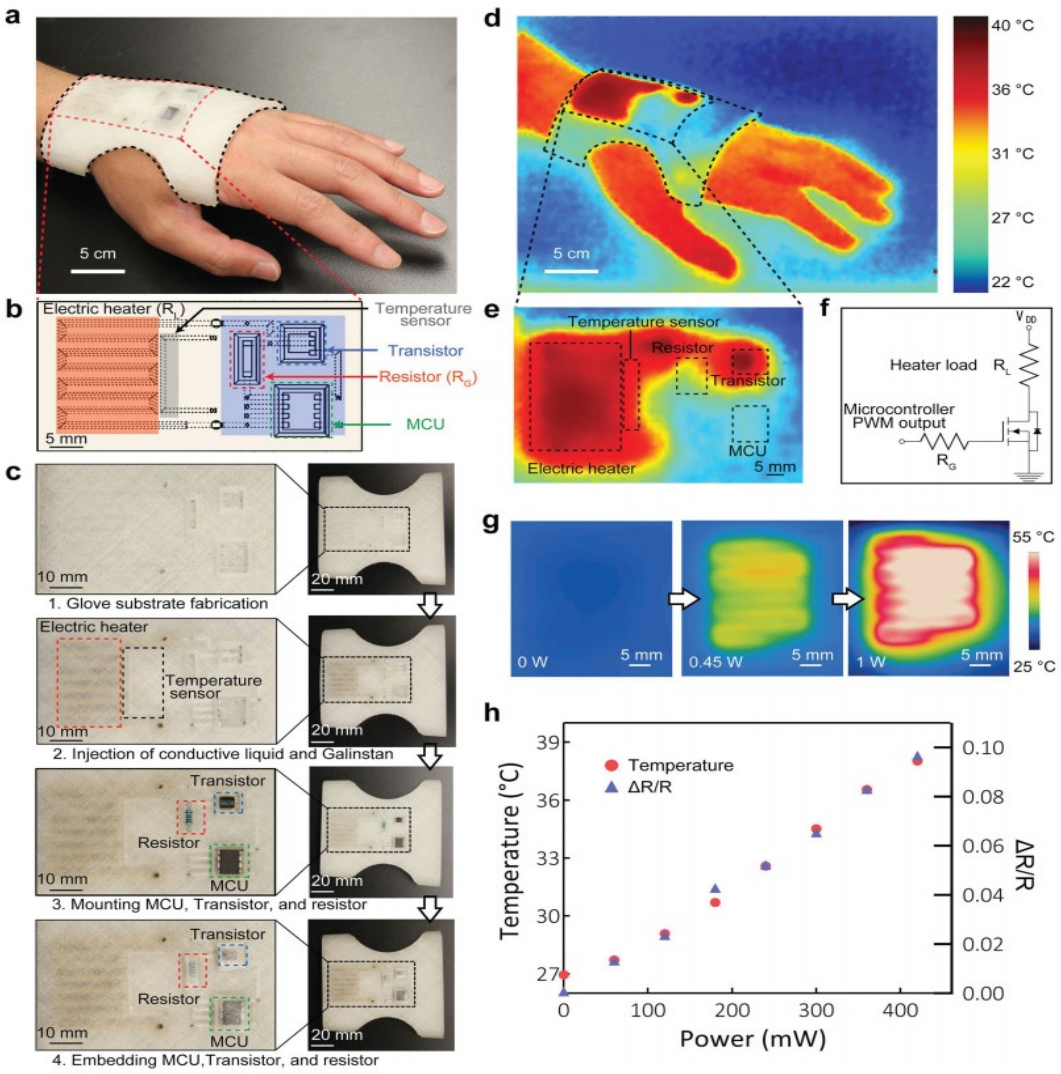

Figure 4. a) Optical image of the fabricated smart glove. b) Layout of the smart glove illustrating the placement of liquid-state heater and temperature sensor, as well as the transistor switch for delivering electrical current through the heater and the MCU to program and control the heat delivery process. c) The fabrication process flow of the smart glove. d) Thermography of the worn glove while powered on. e) Corresponding magnified image of the functional part of the glove during its active operation. f) Circuit diagram of the programmable power delivery to the heater based on the pulse width modulation (PWM) technique. g) High magnification thermography of the heater at different power levels (left image: 0 W; center image: 0.45 W; right image: 1 W). h) Temperature increase of the heater region with increase in heater power. Here, the temperature is measured by infrared imaging (left axis) and by recording the increase in resistance (ΔR) of the temperature sensor as normalized with respect to the temperature sensors' resistance at room temperature with no heat delivery (R).

Figure 4c shows the fabrication process of the glove. This procedure includes 3D embedding of the liquid metal based heater and temperature sensor. The process also integrates a transistor switch to power the heater and an MCU to program and control the heat delivery (more details in the Experimental Section; Figures S10 and S11, Supporting Information). Figure 4d,e shows infrared images of the glove being worn during the heat delivery and the resultant temperature profile. Figure 4f illustrates the corresponding circuit schematic for the programmable heat delivery system. As verified both by infrared imaging and the integrated temperature sensor measurements, the temperature of the heater can be linearly modulated through programming the input power (Figure 4g,h). This programmability feature provides a precise control in heat delivery which is critical for the intended application.

Here, as a proof-of-concept, we demonstrated the temperature sensing and heat delivery capability of the glove. We can extend the utility of such point-of-care printable devices to other relevant therapeutic and health monitoring applications such as wound healing and drug delivery by integrating the required functionalities (e.g., pH and humidity sensing and optical imaging).

In summary, we have demonstrated the capability of the 3D printing approach to deliver fully integrated personalized smart objects. The presented process integrates the liquid-state printed components with the readily available silicon IC chips in all three dimensions and multiple printing layers to develop fully embedded electronic and sensing systems with advanced functionalities (e.g., photodetection and programmable heat delivery). This approach provides new degrees of freedom in the electrical and mechanical design of embedded systems as compared to that offered by the printed circuit board (PCB) technologies. The fabrication process is scalable in terms of packing more advanced electronic systems. Here, we were constrained by the resolution of our printer (minimum channel width: 300 µm). In the future, photopolymerization 3D printing technique[28] can potentially be adopted to reduce the minimum feature size of the liquid metal patterns well below the minimum trace widths in PCBs which are on the order of 100 µm. Moreover, the process can synergistically be combined with the previously presented devices for wearable,[29-33] medical,[34-41] and soft robotics[42-46] applications in order to realize their intended full system-level functionalities.

Experimental Section

3D *Printing*: First, the 3D computer-aided design (CAD) data for each device were created using SolidWorks 2014 (SolidWorks Corp.) or Pro/engineer (PTC). The STL file based on the 3D CAD data was transferred to the Simplify3D software (Simplify3D). The printing was performed by a 3D printer via Simplify3D. An M2 3D printer (MakerGear) was used for printing the stretchable 3D material (Filaflex, Recreus). The nozzle diameter was 350 µm. The thickness of each layer was 100 µm. The interior fill percentage was 100 %. The hot-end and stage temperatures were 240 and 40 °C, respectively, with a gap distance of 180 µm between the hot-end and stage. The printing speed was 1500 mm min^{-1} with *X*/*Y* axis movement speed set to 3000 mm min^{-1}.

For the 3D printing using the solid material, polylactic acid (Leapfrog) was printed with the aid of a Creatr HS (Leapfrog) 3D printer. The hot-end and stage temperature were 225 and 45 °C, respectively. The printing speed was 3000 mm min^{-1} with *X*/*Y* axis movement speed set to 3000 mm min^{-1}. Other parameters were same as those of the M2 printer.

Fabrication of Twistable LED and Light Intensity Measurement during Twisting: The cylindrical substrate of the twistable LED was made of Filaflex using the M2 printer. After printing the substrate, Galinstan (Rotometal) was injected from the inputs using a syringe. Afterward, a red LED was connected

to the input holes on the other side. In order to observe the effect of twisting, one side of the device was clamped on a table while the other side was connected with a rotation tool. A power meter (PM100D, Thorlabs) was set at the vicinity of the LED to quantify the power of the emitted light.

Fabrication, Characterization, and Application of 3D Printed Antennas: The substrates containing the microchannels for the dipole antennas were made of Filaflex using the M2 printer. After printing, Galinstan was injected into the channels. Each antenna was connected to a SubMiniature version A (SMA) connector (Pomona) and was characterized by a network analyzer (E5071C, Agilent) to measure the ratio of power reflected by the antenna to the power incident to the antenna (i.e., S_{11}). An efficient dipole antenna should radiate maximally at its resonance frequency, which corresponds to a notch at the resonance frequency in the S_{11} curve for the antenna. The tunability of the 3D printed antennas was also characterized by fabricating dipole antennas of various lengths. Resonant frequencies for the antennas were determined by the frequencies of the notch in their respective S_{11} curves. In order to observe actual transmission of data and based on the antenna characterization results (Figure 2d), the 3D printed 24.5 mm antennas were installed into a receiver (RC805, Boscam) and a transmitter (TS351, Boscam). By connecting the transmitter and receiver with a laptop and a digital camera (PowerShot SX230 or Canon EOS KissX3, Canon Inc.), a video signal was transmitted and displayed.

Fabrication of 3D Printed Cylindrical Liquid-State Low- or High-Pass Filter and Filter Functionality Measurement: The cylindrical low- and high-pass filters containing microchannels for liquid-state resistors and capacitors were made of Filaflex using the M2 printer. After the printing step, the resistor channel was filled with silicone oil containing 20% carbon black (MG Chemicals) by injection. Next, Galinstan was injected into the inner and outer channels of the capacitor portion of the cylindrical filter. Characterization of the impedance of the fabricated circuit elements (resistor and capacitor) as well as the filter frequency response was performed by an impedance spectroscope (HF21S Impedance Spectroscope, Zurich Instrument). In order to achieve a range of silicone oil (Sigma Aldrich) conductivities (Supporting Information Figure S4c), different additives were used including silver microparticles (AgMPs, Sigma Aldrich), multiwall carbon nanotubes (Cheaptubes.com), and carbon black. In each case, the additive of interest was mixed into the silicone oil manually.

Fabrication of 3D Printed Electronic Systems: To demonstrate our process capability for 3D printing of electronic systems, a 3-layer signal conditioning and processing unit was printed to implement a photodetection system using the Creatr HS printer. For this fabrication process, the stage temperature should be maintained at 45 °C to prevent detachment of the structure from the stage. Upon completion of printing of each layer, the printing process was paused to inject Galinstan into each channel and to insert the required circuit components into their designated positions. In order to obtain a flat

top layer, PDMS and then epoxy resin were poured onto the inserted components. The 3D fabrication process was then continued by modifying the G-code to print the subsequent layers in the design and repeating the previous steps. The system is primarily composed of a TIA, an LPF, and a microcontroller. The TIA and LPF are implemented with a TLV2402 operational amplifier (Texas Instruments). An LED light source is used to illuminate a phototransistor (ALS-PT243-3C/L177, Everlight Electronics) which transduces current level proportional to the input light intensity. The TIA converts this current to a voltage, and the LPF filters out high-frequency noise. The filtered voltage is read by the analog-to-digital converter of the microcontroller (ATTINY85 by Atmel Corp.) with 10-bit resolution and displayed with the aid of an LED as a series of pulses. The microcontroller is programmed using an external Arduino Uno (Arduino, LLC) development board. Power is supplied by two lithium polymer batteries with nominal voltages of 3.7 V.

Fabrication of the 3D Printed Glove: The 3D printing was done using the M2 printer with the same process flow as the 3D current sensor. In order to control the temperature of the electric heater, a pulse width modulation (PWM) system composed of a microcontroller (ATTINY85 by Atmel Corp.), metal-oxide-semiconductor field effect transistor (MOSFET, BS270 by Fairchild Semiconductor), and resistor was utilized. The microcontroller was programmed to output a PWM signal with a configurable duty cycle. The duty cycle can be set by reprogramming the microcontroller using an external Arduino Uno development board. The development board can then be detached for standalone operation. The PWM signal is connected to the gate of the MOSFET, which modulates the current through the printed heating element to achieve a desired power output. Power was supplied by a lithium polymer battery with a nominal voltage of 3.7 V.

Viscosity Measurement of Conductive Liquid With Respect To the Ratio of AgMP: Interfacial dynamic shearing viscosities of the conductive liquids were determined by a stress controlled oscillatory rheometer (Physica MCR 302 Modular Compact Rheometer, Anton Paar, Ashland, VA) with 25 mm parallel plates, gap height of 0.5 mm, 5 Hz, and 0.5% strain at 25 °C. Samples with different AgMP ratios were loaded between the plates and measurements were performed.

Acknowledgements

H.O. and S.E. contributed equally to this work. This work was supported by the NSF NASCENT Center, National Institutes of Health Grant P01 HG000205, and the Director, Office of Science, Office of Basic Energy Sciences, Material Sciences and Engineering Division of the U.S. Department of Energy under Contract No. DE-AC02-05CH11231. H.O. acknowledges support from the Japan Society for the Promotion of Science (JSPS) Fellowship. Y.G. acknowledges support from the China Scholarship Council (File No. 201406250097). The authors thank J. Lotz, K. Gary, Y. Leng, the staff in

CITRIS INVENTION LAB of University of California, Berkeley, and Electronic Materials Program (E-Mat) of Lawrence Berkeley National Laboratory for their help.

References

[1] K. David , S. Dixit , N. Jefferies , IEEE Trans. Veh. Technol. 2010 , 5 , 22 . [2] J. A. Lewis , B. Y. Ahn , Nature 2015 , 518 , 42 . [3] B. H. Kim , M. S. Onses , J. B. Lim , S. Nam , N. Oh , H. Kim , K. J. Yu , J. W. Lee , J.-H. Kim , S.-K. Kang , C. H. Lee , J. Lee , J. H. Shin , N. H. Kim , C. Leal , M. Shim , J. A. Rogers , Nano Lett. 2015 , 15 , 969 . [4] J. T. Muth , D. M. Vogt , R. L. Truby , Y. Mengüç , D. B. Kolesky , R. J. Wood , J. A. Lewis , Adv. Mater. 2014 , 26 , 6307 . [5] L. E. Bertassoni , M. Cecconi , V. Manoharan , M. Nikkhah , J. Hjortnaes , A. L. Cristino , G. Barabaschi , D. Demarchi , M. R. Dokmeci , Y. Yang , A. Khademhosseini , Lab Chip 2014 , 14 , 2202 . [6] L. E. Bertassoni , J. C. Cardoso , V. Manoharan , A. L. Cristino , N. S. Bhise , W. A. Araujo , P. Zorlutuna , N. E. Vrana , A. M. Ghaemmaghami , M. R. Dokmeci , A. Khademhosseini , Biofabrication 2014 , 6 , 024105 . [7] B. Y. Ahn , E. B. Duoss , M. J. Motala , X. Guo , S.-I. Park , Y. Xiong , J. Yoon , R. G. Nuzzo , J. A. Rogers , J. A. Lewis , Science 2009 , 323 , 1590 . [8] Y. L. Kong , I. A. Tamargo , H. Kim , B. N. Johnson , M. K. Gupta , T.-W. Koh , H.-A. Chin , D. A. Steingart , B. P. Rand , M. C. McAlpine , Nano Lett. 2014 , 14 , 7017 . [9] J. W. Boley , E. L. White , G. T.-C. Chiu , R. K. Kramer , Adv. Funct. Mater. 2014 , 24 , 3501 . [10] Y.-L. Park , C. Majidi , R. Kramer , P. Bérard , R. J. Wood , J. Micromech. Microeng. 2010 , 20 , 125029 . [11] S.-Y. Wu , C. Yang , W. Hsu , L. Lin , Microsyst. Nanoeng. 2015 , 1 , 15013 . [12] M. D. Dickey , R. C. Chiechi , R. J. Larsen , E. A. Weiss , D. A. Weitz , G. M. Whitesides , Adv. Funct. Mater. 2008 , 18 , 1097 . [13] R. K. Kramer , C. Majidi , R. J. Wood , Adv. Funct. Mater. 2013 , 23 , 5292 . [14] J. Park , S. Wang , M. Li , C. Ahn , J. K. Hyun , D. S. Kim , D. K. Kim , J. A. Rogers , Y. Huang , S. Jeon , Nat. Commun. 2012 , 3 , 916 . [15] A. Tabatabai , A. Fassler , C. Usiak , C. Majidi , Langmuir 2013 , 29 , 6194 . [16] S. Cheng , A. Rydberg , K. Hjort , Z. Wu , Appl. Phys. Lett. 2009 , 94 , 144103 . [17] S. Cheng , Z. Wu , Lab Chip 2010 , 10 , 3227 . [18] M. Kubo , X. Li , S. Kim , M. Hachimoto , B. J. Wiley , D. Ham , G. M. Whitesides , Adv. Mater. 2010 , 22 , 2749 . [19] G. J. Hayes , S. C. Desai , Y. Liu , P. Annamaa , G. Lazzi , M. D. Dickey , Microwave Opt. Technol. Lett. 2014 , 56 , 1459 . [20] G. J. Hayes , J.-H. So , A. Qusba , M. D. Dicky , G. Lazzi , IEEE Trans. Antennas Propag. 2012 , 60 , 2151 . [21] A. Qusba , A. Kumar , R. Rakhyani , J.-H. So , G. J. Hayes , M. D. Dicky , G. Lazzi , IEEE Sens. 2014 , 14 , 1074 . [22] M. Li , B. Yu , N. Behdad , IEEE Microwave Wireless Components Lett. 2012 , 20 , 423 . [23] J. Wang , S. Liu , Z. V. Vardeny , A. Nahata , Optics Express 2012 , 20 , 2346 . [24] J. Wang , S. Liu , Z. V. Vardeny , A. Nahata , Optics Express 2012 , 20 , 12119 . [25] J.-H. So , J. Thelen , A. Qusba , G. J. Hayes , G. Lazzi , M. D. Dickey , Adv. Funct. Mater. 2009 , 19 , 3632 . [26] R. D. Ponce Wong , J. D. Posner , V. J. Santos , Sens. Actuators A: Phys. 2012 , 179 , 62 . [27] S. Michlovitz , L. Hun , G. N. Erasala , D. A. Hengehold , K. W. Weingand , Arch. Phys. Med. Rehabil. 2004 , 85 ,

1409 . [28] I. Aharonovich , J. C. Lee , A. P. Magyar , B. B. Buckley , C. G. Yale , D. D. Awschalom , E. L. Hu , Adv. Mater. 2012 , 24 , OP54 . [29] A. P. Magyar , D. Bracher , J. C. Lee , I. Aharonovich , E. L. Hu , Appl. Phys. Lett. 2014 , 104 , 051109 . [30] A. Woolf , T. Puchtler , I. Aharonovich , T. Zhu , N. Niu , D. Wang , R. Oliver , E. L. Hu , Proc. Natl. Acad. Sci. USA 2014 , 111 , 14042 . [31] W. Zhou , S. M. Kuebler , K. L. Braun , T. Yu , J. K. Cammack , C. K. Ober , J. W. Perry , S. R. Marder , Science 2002 , 296 , 1106 . [32] D. J. Lipomi , M. Vosgueritchian , B. C.-K. Tee , S. L. Hellstrom , J. A. Lee , C. H. Fox , Z. Bao , Nat. Nano 2011 , 6 , 788 . [33] M. Vosgueritchian , J. B.-H. Tok , Z. Bao , Nat. Photon. 2013 , 7 , 769 . [34] G. Schwartz , B. C.-K. Tee , J. Mei , A. L. Appleton , D. H. Kim , H. Wang , Z. Bao , Nat. Commun. 2013 , 4 , 1859 . [35] S. Xu , Y. Zhang , L. Jia , K. E. Mathewson , K.-I. Jang , J. Kim , H. Fu , X. Huang , P. Chava , R. Wang , S. Bhole , L. Wang , Y. J. Na , Y. Guan , M. Flavin , Z. Han , Y. Huang , J. A. Rogers , Science 2014 , 344 , 70 . [36] Y. Kim , J. Zhu , B. Yeom , M. Di Prima , X. Su , J.-G. Kim , S. J. Yoo , C. Uher , N. A. Kotov , Nature 2013 , 500 , 59 . [37] P.-K. Yang , L. Lin , F. Yi , X. Li , K. C. Pradel , Y. Zi , C.-I. Wu , J.-H. He , Y. Zhang , Z. L. Wang , Adv. Mater. 2015 , 27 , 3817 . [38] B. Tian , J. Liu , T. Dvir , L. Jin , J. H. Tsui , Q. Qing , Z. Suo , R. Langer , D. S. Kohane , C. M. Lieber , Nat. Mater. 2012 , 11 , 986 . [39] J. Liu , T.-M. Fu , Z. Cheng , G. Hong , T. Zhou , L. Jin , M. Duvvuri , Z. Jiang , P. Kruskal , C. Xie , Z. Suo , Y. Fang , C. M. Lieber , Nat. Nano 2015 , 10 , 629 . [40] C. Dagdeviren , Y. Shi , P. Joe , R. Ghaffari , G. Balooch , K. Usgaonkar , O. Gur , P. L. Tran , J. R. Crosby , M. Meyer , Y. Su , R. Chad Webb , A. S. Tedesco , M. J. Slepian , Y. Huang , J. A. Rogers , Nat. Mater. 2015 , 14 , 728 . [41] H. Zhang , P. R. Patel , Z. Xie , S. D. Swanson , X. Wang , N. A. Kotov , ACS Nano 2013 , 7 , 7619 . [42] H. Zhang , J. Shih , J. Zhu , N. A. Kotov , Nano Lett. 2012 , 12 , 3391 . [43] W. Tang , J. Tian , Q. Zheng , L. Yan , J. Wang , Z. Li , Z. L. Wang , ACS Nano 2015 , 9 , 7867 . [44] J. Liu , C. Xie , X. Dai , L. Jin , W. Zhou , C. M. Lieber , Proc. Natl. Acad. Sci. USA 2013 , 110 , 6694 . [45] R. F. Shepherd , F. Ilievski , W. Choi , S. A. Morin , A. A. Stokes , A. D. Mazzeo , X. Chen , M. Wang , G. M. Whitesides , Proc. Natl. Acad. Sci. USA 2011 , 108 , 20400 . [46] R. V. Martinez , J. L. Branch , C. R. Fish , L. Jin , R. F. Shepherd , R. M. D. Nunes , Z. Suo , G. M. Whitesides , Adv. Mater. 2013 , 25 , 205 .